Numerical Investigation of Flow Structures and Interactions due to a Pitched Synthetic Jet in a Laminar Boundary Layer

Jason Li* and Onkar Sahni†

Department of Mechanical, Aerospace, and Nuclear Engineering,

Rensselaer Polytechnic Institute, Troy, NY, 12180, United States

A numerical investigation is conducted to study flow structures and interactions that are caused by a pitched synthetic jet placed in a laminar (Blasius) boundary layer with zero pressure gradient. Simulations are performed for various permutations of jet parameters including pitch angle (i.e., θ=60^o, 75^o, and 90^o), blowing ratio (i.e., C_b = 0.5, 1.0, 1.5, and 2.0), and non-dimensional actuation frequency (i.e., $\hat{f}_{jet}$=0.05, 0.1, 0.2, and 0.4). Cases corresponding to the full set of jet parameters are studied based on 2D simulations while, for selected cases, 3D simulations are also considered. In these cases, we focus on five flow structures and behaviors: a discrete train of vortex pairs, subharmonics, vortex pair switching, vortex splitting, and complex vortex interactions.

Nomenclature

C_b	Blowing ratio of the synthetic jet
$\delta_{orifice}$	Boundary layer thickness at the jet orifice
U_∞	Crossflow velocity
d	Jet orifice and neck width (with respect to normal of the jet neck walls)
f_{ref}	Reference frequency
f_{jet}	Actuation frequency of the synthetic jet
$\hat{f}_{jet}$	Non-dimensional jet frequency
ω	Spanwise vorticity
ω_{wall}	Spanwise vorticity at the wall
Re_δ	Reynolds number based on boundary layer thickness
θ	Pitch angle of the synthetic jet
$\langle \bar{V}_{jet} \rangle$	Spatial-temporal average of the jet exit velocity

I. Introduction

Flow control is a growing field of research with many potential applications in both commercial and military use. Many studies have demonstrated the ability for both passive and active flow mechanisms to alter the fluid flow behavior and yield desirable results. The use of passive mechanisms often creates additional drag, so active mechanisms are favorable for certain applications.[2,3,11] However, for active mechanisms to be efficient, they must be easily implemented, use a low amount of input energy, and provide the required level of actuation. One such flow control device is the synthetic jet,[5] a zero-net-mass-flux fluidic actuator that operates at a range of frequencies. Synthetic jets are practical to implement and, due to the use of a resonance mechanism, require only a low energy input and are also physically compact.[4] Various applications of synthetic jets have been considered and tested. Such applications include, for example, delay of flow separation on airfoils at high angles of attack,[1] fluidic thrust vectoring,[12] virtual aeroshaping,[9] etc.

*Graduate Student, Rensselaer Polytechnic Institute

†Assistant Professor, Rensselaer Polytechnic Institute, AIAA Senior Member

In this study, we focus on the interactions of a pitched synthetic jet with a non-separated crossflow or a boundary layer flow. Under certain jet parameters, the crossflow may experience a virtual bubble or hump in a time-averaged sense due to which the crossflow streamlines bend and cluster, as depicted in Figure 1.[9]

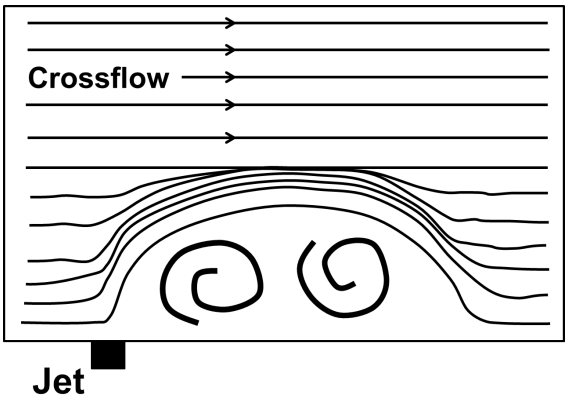

Figure 1: Schematic of the virtual aeroshaping effect

Virtual aeroshaping changes the aerodynamic performance due to the resulting change in the local pressure gradient, for example. Therefore, control over the extent of flow structures and interactions allows for the control of aerodynamic performance. In order to control flow structures due to actuation, it becomes necessary to identify and understand how actuator parameters (both geometric and operational parameters) affect the interactions of the synthetic jet with the crossflow. Honohan et al.[7] created a parametric map on the closure of the virtual recirculation bubble due to different combinations of blowing ratio and frequencies. A schematic is shown in Figure 2. In this work, we use numerical simulations to study pitched synthetic jets by analyzing different vortical structures and behaviors that occur due to variation in actuation parameters. We do this first with the help of 2D simulations at various jet parameters and for selected cases 3D simulations are also considered.

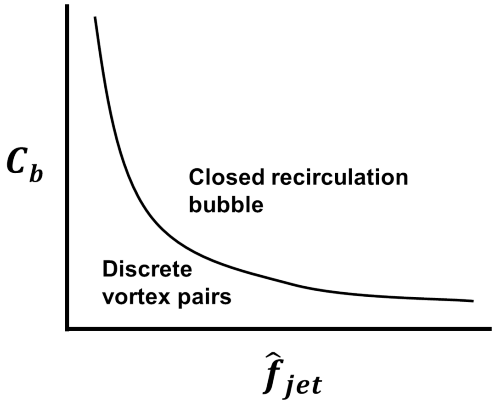

Figure 2: Schematic of a parametric map of resulting flow structures and interactions

This paper is organized as follows. Section II discusses the numerical methodology used in the simulations. Section III presents numerical results where different vortical structures and behaviors are discussed. Section IV summarizes the work and discusses possible future work.

II. Numerical Methodology

The flow solver used in this work is based on the incompressible Navier-Stokes equations and employs a stabilized finite element method[13] along with an implicit generalized-α time integration technique.[8]

In current simulations, a synthetic jet actuator is placed in a Blasius boundary layer flow. The computational domain is composed of a rectangular section with a synthetic jet attached at the bottom wall, as shown in Figure 3a and Figure 3b. At the inlet, a Blasius velocity profile is prescribed such that the boundary layer thickness at the center of the jet orifice is $\delta_{orifice}$=5.0mm; the orifice is located at a distance of 20.32mm from the inlet. Similarly, a velocity profile is prescribed at the top boundary of the domain; the height of the domain is 10.16mm. The jet neck and orifice have a width of d = 1.0mm (with respect to the normal of the jet neck walls) and the height of the jet neck is 6.0mm. The jet cavity has a width of 36.8mm and a height of 2.0mm. At the location of the piezoelectric membrane of the actuator, a plug velocity profile in space whose amplitude varies sinusoidally in time is prescribed (see Figure 3a).

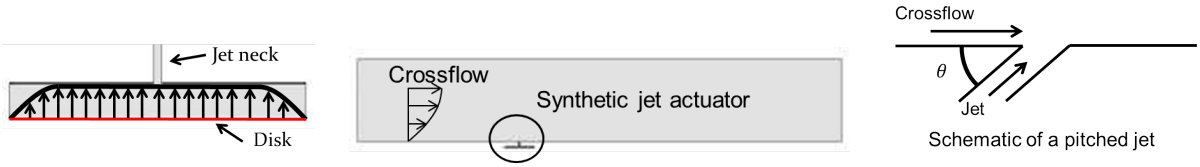

(a) Synthetic jet cavity and neck (for 90^o pitch case)

(b) Computational domain

(c) Schematic of a pitched jet

Figure 3: Model used in simulations

A boundary layer grid is used with a layered mesh generated on top of the bottom wall as well as on the jet neck and cavity walls. The height of the first layer is 0.05mm with eleven layers in total for the bottom wall and four layers on the walls of the neck and cavity, where a growth ratio of about 1.4 is used. The overall grid is shown in Figure 4a. It can be seen that grid resolution near the jet orifice is kept relatively fine by defining refinement zones in this area (a zoomed-in view is shown in Figure 4b). In the inner most refinement zone, the grid size is such that approximately 20 mesh points are placed across the orifice width, and the other refinement zones are progressively coarser by a factor of two. The resulting grid consists of approximately one million cells in total. All cases are run with a time-step size such that there are 180 time steps per jet cycle. Current grid size and temporal resolution are found to be sufficient in our simulations. In 3D simulation cases, the depth of domain is fixed at 5.0mm (i.e., 5d) and the grid consists of 20 layers in the depth. This results in a 3D mesh with approximately 20 million elements. Note that 3D cases correspond to a jet orifice with infinite span, i.e., periodic boundary conditions are used on the sides of the domain. Only certain jet parameters are considered in 3D, where the idea is to study the most interesting 2D cases in order to establish the existence of similar flow structures and behaviors in 3D.

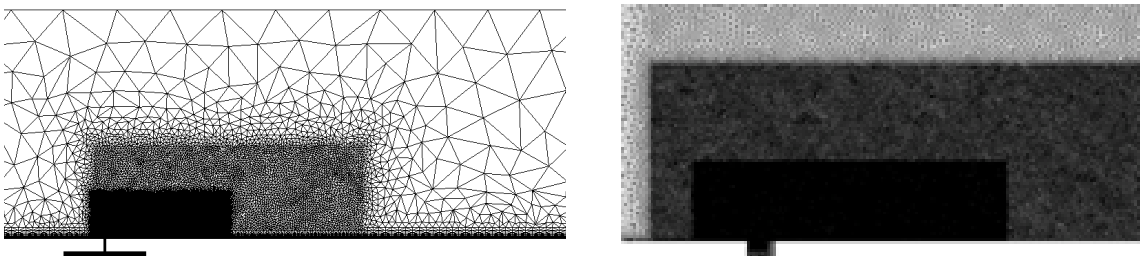

(a) Overall mesh

(b) Refinement zones around jet orifice

Figure 4: Views of mesh used in simulations

III. Results

All simulations are performed at a Reynolds number of Re_δ=2000 (based on the crossflow velocity, U_∞, and the boundary layer thickness at the jet orifice, $\delta_{orifice}$). In these simulations, different permutations of pitch angle (of the synthetic jet actuator) along with actuation frequency and blowing ratio are considered. Three pitch angles are considered: θ=60^o, 75^o, and 90^o, where the angle is measured with respect to the streamwise direction, as depicted in Figure 3c, and a jet with pitch angle of 90^o is normal to the crossflow. Note that the width and length of the neck remain constant while the orifice width changes with the pitch angle. Four non-dimensional jet frequencies, $\hat{f}_{jet}$=0.05, 0.1, 0.2, and 0.4, are considered, where

$\hat{f}_{jet} = f_{jet}/f_{ref}$, and $f_{ref} = U_\infty/d$. Four blowing ratios of C_b = 0.5, 1.0, 1.5, and 2.0, are also considered, where $C_b = \langle \bar{V}_{jet} \rangle / U_\infty$. Here, $\langle \bar{V}_{jet} \rangle$ is the spatial-temporal average of the jet exit velocity (i.e., at the orifice).

Flow structures and interactions are studied and analyzed based on instantaneous (spanwise) vorticity data, which is collected over multiple jet cycles from each simulation. The evolution of vortical structures is described based on this data. We focus on selected structures and interactions including: a discrete train of vortex pairs, subharmonic behavior of vortical structures, vortex pair switching, vortex splitting, and complex vortex interactions. For 2D cases, each such structure and interaction is presented for a certain value of C_b and $\hat{f}_{jet}$ but for all three values of jet pitch angle. While in 3D, all but complex vortex interactions are considered for a particular value of the jet pitch angle (for which the specific type of interaction is most prominent). These are summarized in Table 1, where a pitch value in bold indicates the particular value of the jet pitch angle for 3D simulations.

Table 1: List of jet parameter values for flow interactions

Flow interaction	Jet parameter values
Discrete train of vortex pairs	$C_b = 0.5; \hat{f}_{jet} = 0.20; \theta = \mathbf{60^o}, 75^o, 90^o$
Subharmonics	$C_b = 0.5; \hat{f}_{jet} = 0.10; \theta = 60^o, 75^o, \mathbf{90^o}$
Vortex pair switching	$C_b = 1.0; \hat{f}_{jet} = 0.10; \theta = 60^o, \mathbf{75^o}, 90^o$
Vortex splitting	$C_b = 1.0; \hat{f}_{jet} = 0.05; \theta = \mathbf{60^o}, 75^o, 90^o$
Complex vortex interactions	$C_b = 2.0; \hat{f}_{jet} = 0.10; \theta = 60^o, 75^o, 90^o$

III.A. Discrete Train of Vortex Pairs

The discrete train of vortex pairs is depicted in Figure 5, where vortex pairs are formed every jet cycle which advect with the crossflow and dissipate downstream. These structures are observed for low C_b and higher $\hat{f}_{jet}$. The low C_b has small influence on the crossflow, resulting in minimal interactions between the vortex pairs and the crossflow. The higher actuation frequency injects the vortex pairs into the crossflow with a higher velocity, which facilitates formation and inhibits interactions between other vortex pairs.

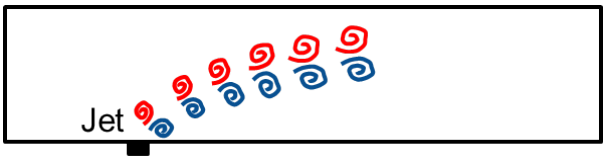

Figure 5: Depiction of a discrete train of vortex pairs

This behavior is clearly observed in the case with $\theta = 60^o$ with C_b=0.5, and $\hat{f}_{jet}$=0.2, as shown by the instantaneous vorticity contours in Figure 6, where ω, the spanwise vorticity, is normalized by ω_{wall}, the spanwise vorticity at the wall at the location of the orifice generated by the baseline crossflow, i.e., due to the Blasius boundary layer. At $\theta = 60^o$ pitch, the vortex pairs are injected with a velocity component which has some alignment with the crossflow. This enhances the advection of vortex pairs.

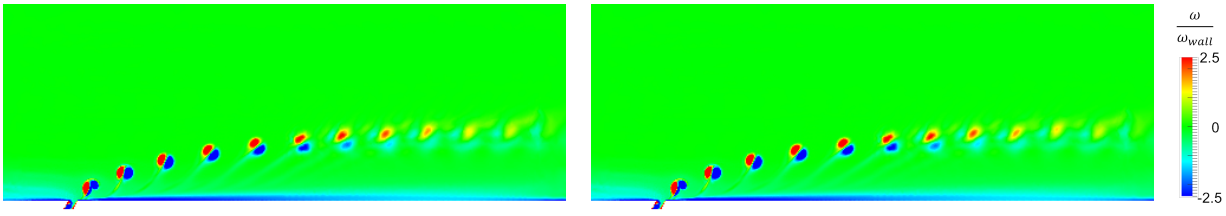

(a) Cycle A, Phase 360 (b) Cycle B, Phase 360

Figure 6: Discrete train of vortex pairs for $\theta = 60^o$, C_b=0.5, $\hat{f}_{jet}$=0.2

A train of vortices, dominated by clockwise vortices (in blue), is observed for $\theta = 75^o$ for the same value of C_b and $\hat{f}_{jet}$ (see Figure 7). However, a clear train of vortex pairs is not observed since the normal component of the velocity to the crossflow of the injected vortex pairs is greater than for $\theta = 60^o$, causing

larger interference with the crossflow. Moreover the counter-clockwise vortex (in red) from a given jet cycle travels faster and separates from the clockwise vortex (in blue) of the same jet cycle. The higher pitched jet causes the crossflow to experience a stronger "wall"-like structure due to local blockage caused by the jet (in a time-averaged sense), resulting in a recirculation zone just downstream of the jet. The clockwise vortices are injected into this recirculation zone and travel with a lower velocity than the counter-clockwise vortices that experience higher crossflow velocity. This causes the counter-clockwise vortices to accelerate past the clockwise vortices.

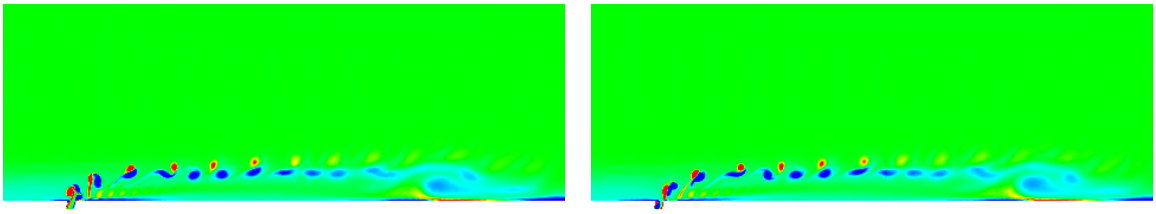

(a) Cycle A, Phase 360 (b) Cycle B, Phase 360

Figure 7: Discrete train of vortex pairs for $\theta = 75^o$, C_b=0.5, $\hat{f}_{jet}$=0.2

Increasing the pitch to $\theta = 90^o$ results in no observable discrete train of vortex pairs. Since vortex pairs are injected normal to the crossflow, the pair has no significant velocity component in the direction of the crossflow. Thus, the vortex pairs are more resilient to advection, and, due to the higher frequency, part of the vortex pairs are ingested back into the actuator cavity during suction part of the jet cycle. As a result, marginal to no formation is achieved, as shown in Figure 8.

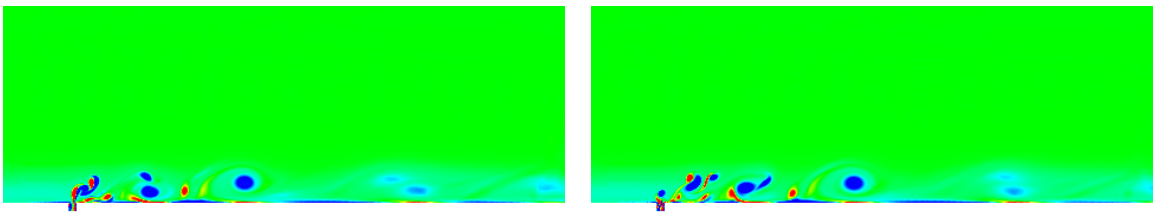

(a) Cycle A, Phase 360 (b) Cycle B, Phase 360

Figure 8: Discrete train of vortex pairs for $\theta = 90^o$, C_b=0.5, $\hat{f}_{jet}$=0.2

III.B. Subharmonics

For cases with low blowing ratio and lower frequency, subharmonic behavior of vortical structures is observed for only a certain pitch angle. An illustration of power spectral density (PSD) is shown for a subharmonic behavior in Figure 9, where the two dominant frequencies correspond to the jet frequency and half of that. Shown in Figure 10 are instantaneous vorticities at the end of four consecutive jet cycles for $\theta = 60^o$, C_b=0.5, and $\hat{f}_{jet}$=0.1. In all four plots, the vortical structures are observed to be nearly identical (i.e., a periodic behavior at jet frequency), which indicates that no subharmonic behavior is present.

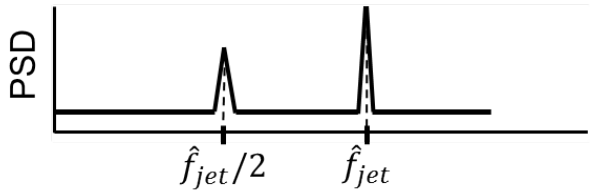

Figure 9: An illustration of power spectral density (PSD) for a subharmonic behavior

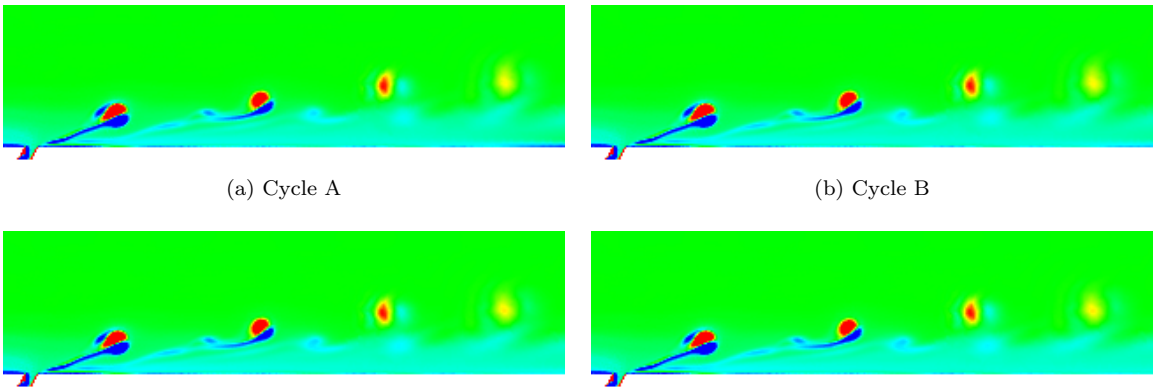

(a) Cycle A (b) Cycle B

(c) Cycle C (d) Cycle D

Figure 10: Subharmonic behavior of vortical structures for $\theta = 60^o$, C_b=0.5, $\hat{f}_{jet}$=0.1

With the same blowing ratio and frequency, the case with $\theta = 75^o$ also does not exhibit subharmonic behavior, as shown in Figure 11.

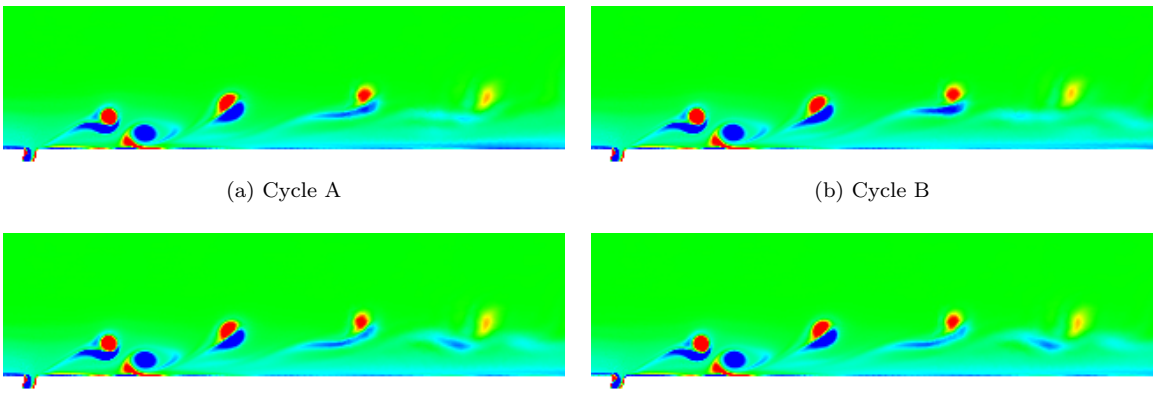

(a) Cycle A (b) Cycle B

(c) Cycle C (d) Cycle D

Figure 11: Subharmonic behavior of vortical structures for $\theta = 75^o$, C_b=0.5, $\hat{f}_{jet}$=0.1

However, increasing the pitch to $\theta = 90^o$ yields a subharmonic behavior. Note that in Figure 12, except for the newly formed vortex pair near the jet, the vortical structures of Cycle A are different from those of Cycle B (i.e., vortical structures at a given phase in the jet cycle are different between two consecutive jet cycles). However, the vortical structures of Cycles A and C are nearly identical, and likewise for Cycles B and D (i.e., vortical structures repeat every other jet cycle). Clearly, there is a subharmonic behavior occurring for the vortex structures with respect to the jet frequency. Note that the newly formed vortex pair repeats every jet cycle, which shows the formation of the jet is not responsible for this behavior. Therefore, subharmonic behavior emanates from downstream interactions between vortex pairs that are from different jet cycles, e.g., due to vortex pair switching as discussed next.

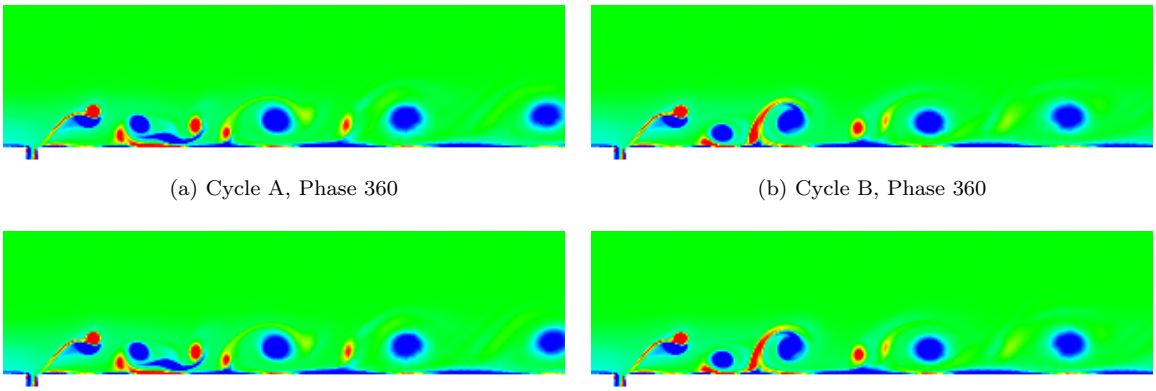

(a) Cycle A, Phase 360

(b) Cycle B, Phase 360

(c) Cycle C, Phase 360

(d) Cycle D, Phase 360

Figure 12: Subharmonic behavior of vortical structures for $\theta = 90^o$, C_b=0.5, $\hat{f}_{jet}$=0.1

III.C. Vortex Pair Switching

In each jet cycle, one vortex pair is formed by the jet and consists of two counter-rotating vortices, one counter-clockwise (red) and one clockwise (blue). Further downstream, vortex pair switching occurs, as shown in Figure 13. In this illustration, vortices from three consecutive jet cycles are shown. The counter-rotating pair CCW3 (counter-clockwise) and CW3 (clockwise) are from the last or third of the three cycles and are recently formed. Downstream, it is shown that CCW2 from the second cycle is paired with CW1 which is from the first cycle. Note that this illustration is shown at an instance when limit cycle behavior has been achieved, i.e., this is not applicable to initial transient behavior or start-up process.

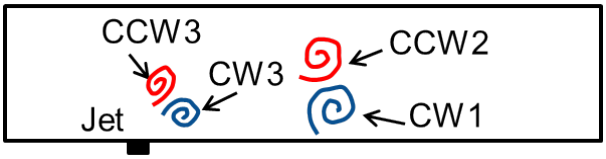

Figure 13: Depiction of vortex pair switching

This behavior is observed for higher blowing ratio and lower frequency. It is possible that this behavior occurs due to the higher blowing ratio. With a higher blowing ratio, the jet exerts a stronger "wall"-like (or local blockage) effect in the crossflow, causing a recirculation zone to form just downstream of the jet. The clockwise vortex of a newly formed pair is formed within this recirculation zone and travels with a slower velocity compared to the crossflow. However, the counter-clockwise vortex experiences faster crossflow, causing it to advect with the crossflow and accelerate over the clockwise vortex. Thus, the counter-clockwise vortex surpasses and separates from the clockwise vortex and pairs with the clockwise vortex from the previous jet cycle. The separation and pairing of individual vortices is expected to contribute to the subharmonic behavior because these phenomena occur at a frequency that is half of that of the jet actuation.

Pair switching is observed for the case with $\theta = 60^o$, C_b=1.0, and $\hat{f}_{jet}$=0.1. In Figure 14, four instantaneous vorticity fields are shown throughout three consecutive jet cycles. Figure 14(a) shows a newly formed vortex pair, CCW2 and CW2, and the vortices CCW1 and CW1 from the previous cycle which have already separated. In the next instance, CCW2 separates from CW2 and appears to pair with CW1 (indicated within the black box). Almost one jet cycle later, the CCW2 and CW1 travel together downstream and travel further away from CW2. The last instance shows CCW2 and CW1 still traveling together, indicating that the two are paired, and by this instance are even further from CW2, indicating that CCW2 and CW2 vortices (i,e., from the same jet cycle) have indeed separated from each other.

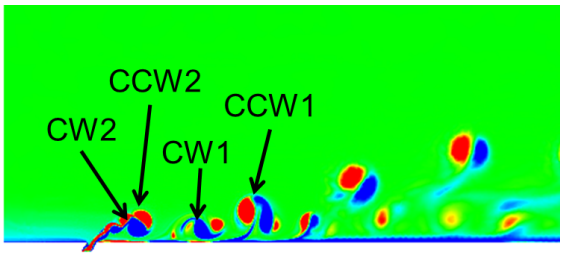

(a) Cycle A, Phase 192

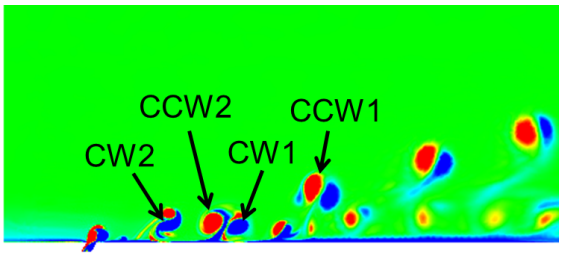

(b) Cycle B, Phase 72

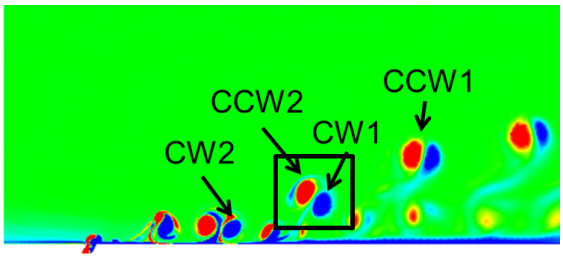

(c) Cycle C, Phase 48

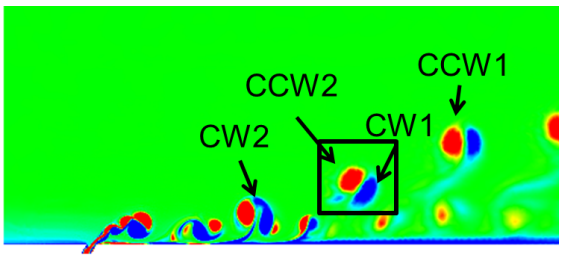

(d) Cycle C, Phase 192

Figure 14: Switching of vortex pair for $\theta = 60^o$, C_b=1.0, $\hat{f}_{jet}$=0.1

For the case with $\theta = 75^o$, and the same blowing ratio and frequency, similar behavior is observed compared with the previous pitch. The newly formed counter-rotating vortex pair separates from each other and join with vortices from different jet cycles. As is seen in Figure 15(a), the pair CCW2 and CW2 form and CCW1 has already separated from CW1. In the next jet cycle, the pair CCW2 and CW2 separate from each other and appears to approach CW1. Near the beginning of the cycle after (in Figure 15(c)), CCW2 and CW1 have paired together (again, indicated within the black box) and appear to have traveled away from CW2. Later in that cycle (in Figure 15(d)), CCW2 and CW1 are still paired, and are further away from CW2, which indicates that CW2 and CCW2 have indeed separated.

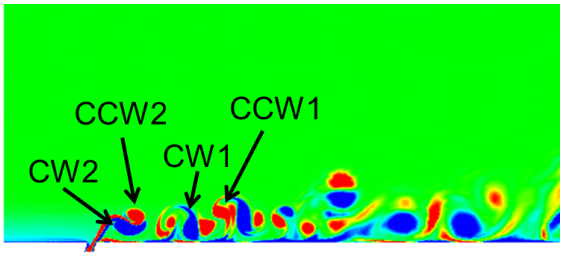

(a) Cycle A, Phase 192

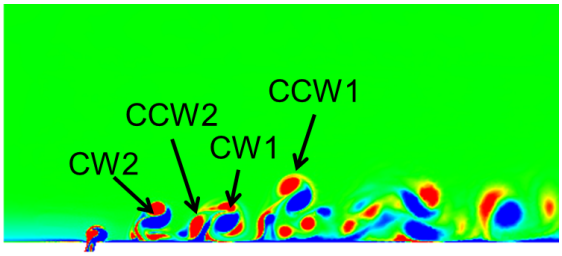

(b) Cycle B, Phase 72

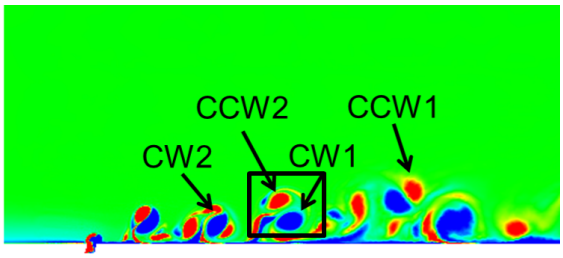

(c) Cycle C, Phase 48

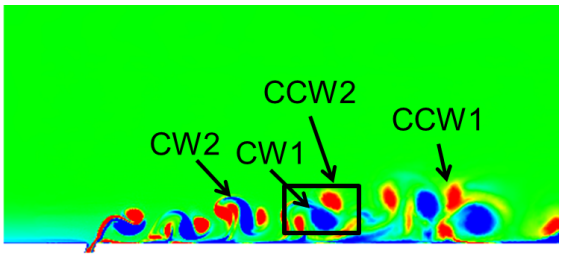

(d) Cycle C, Phase 192

Figure 15: Switching of vortex pair for $\theta = 75^o$, C_b=1.0, $\hat{f}_{jet}$=0.1

The results in the case with $\theta = 90^o$ are very similar. As shown in Figure 16. In the first instance,

CW1 has already separated and the pair CCW2 and CW2 are formed. Then, CCW2 overtakes CW2 and approaches CW1 in the next instance. The pair CCW2 and CW1 form in the instance after. In the last instance, the pair travels further away from CW2, indicating the separation between CCW2 and CW1 as well as the pairing between CCW2 and CW1.

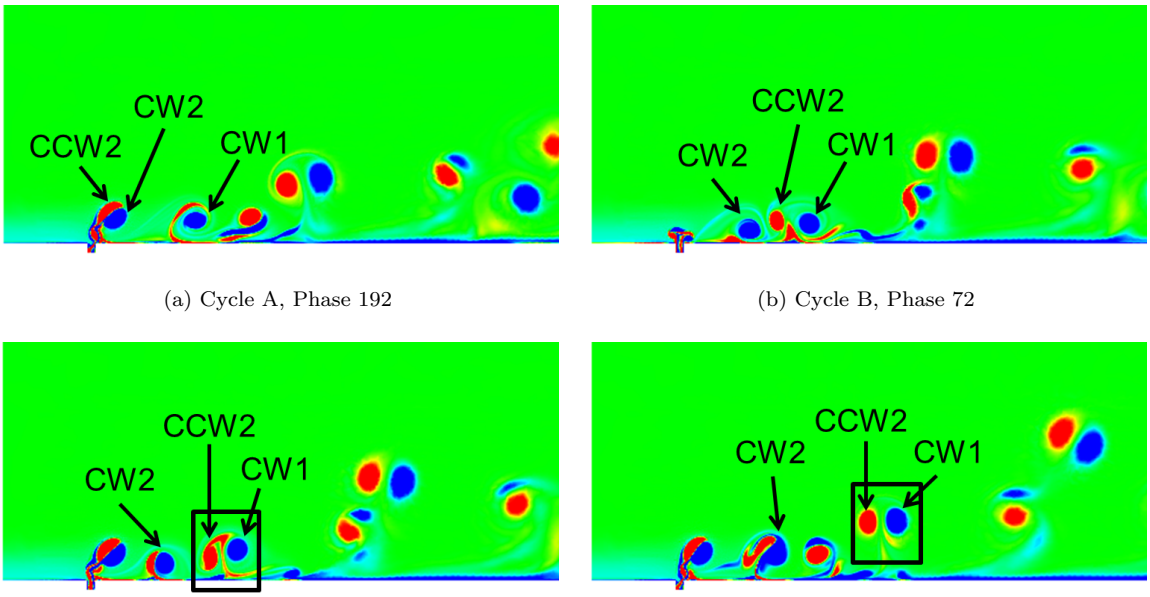

(a) Cycle A, Phase 192

(b) Cycle B, Phase 72

(c) Cycle C, Phase 48

(d) Cycle C, Phase 192

Figure 16: Switching of vortex pair for $\theta = 90^o$, C_b=1.0, $\hat{f}_{jet}$=0.1

III.D. Vortex Splitting

Another behavior observed with vortex pairs is splitting, where due to the crossflow, the newly formed vortices of a jet cycle shear and collide with each other and eventually split into two smaller pairs of counter-rotating vortices or into some other combination. For example, further downstream the two pairs come together in an alternating pattern with respect to the rotation of each vortex, as shown in Figure 17 by the set of vortices CCW1 and CW1 with A and B (where A and B denote the two smaller pairs that form due to the split up of a vortex pair from a given jet cycle).

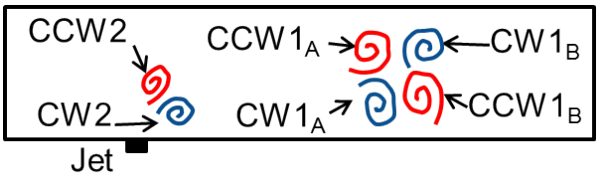

Figure 17: Depiction of vortex splitting

Splitting is observed for cases with a higher blowing ratio and a low frequency. Due to the low frequency, the vortex pair is injected into the crossflow with a low velocity. Instead of the vortices rolling over each other as they do in pair switching, one vortex collides into the other and causes a split. Together with the recirculation zone generated by the higher blowing ratio, complex behavior occurs with the vortical structures which result in the alternating rotation pattern further downstream.

Splitting behavior is observed clearly for the case with $\theta = 60^o$, C_b=0.1, and $\hat{f}_{jet}$=0.05 in Figure 18. Again, four instances or phases of the vorticity field are shown, but these phases are all within a single jet cycle. In the first instance, the vortex pair forms and is sheared by the crossflow. Two pairs of counter-rotating vortices (denoted by A and B) begin to form from the single pair of the current jet cycle. In the next instance, the two pairs are distinct, as shown within the black box, and appear to approach each other in the instance after. At the end of the jet cycle (the last instance), the two pairs are arranged such that each vortex is adjacent to two vortices of opposite rotation.

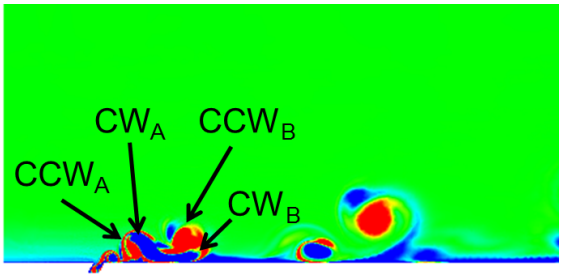

(a) Phase 192

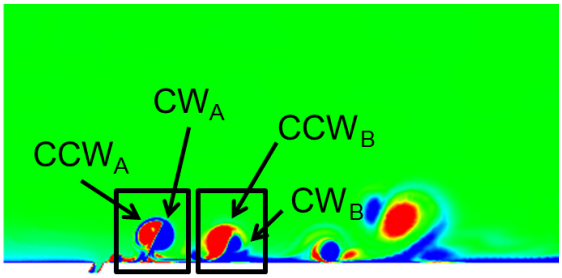

(b) Phase 240

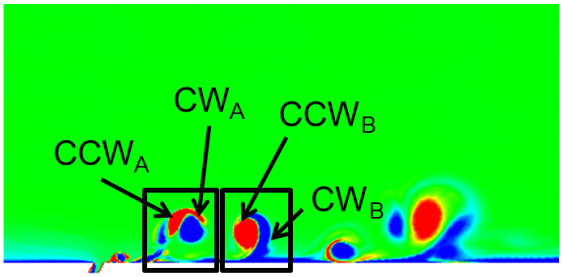

(c) Phase 288

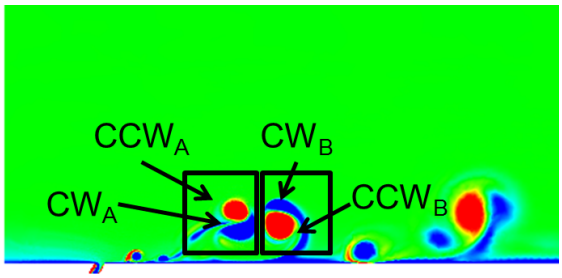

(d) Phase 360

Figure 18: Splitting of vortex pair for $\theta = 60^o$, C_b=1.0, $\hat{f}_{jet}$=0.05

In the case with $\theta = 75^o$, the two pairs are already distinct in the first instance (see Figure 19). The arrangement of opposite rotations occurs in the second instance. In the last instance, the two pairs undergo switching too. This causes CCW_B to pair with CW_A while CCW_A pairs with CW_B (as shown with the black boxes in Figure 19(d)).

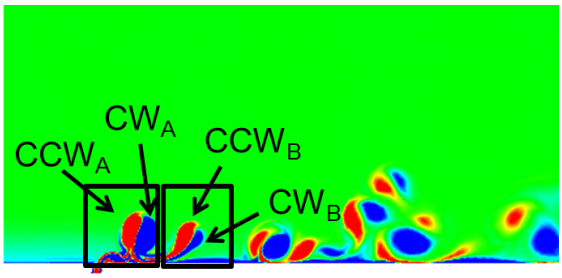

(a) Phase 192

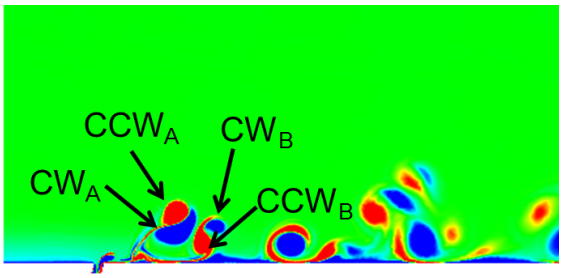

(b) Phase 240

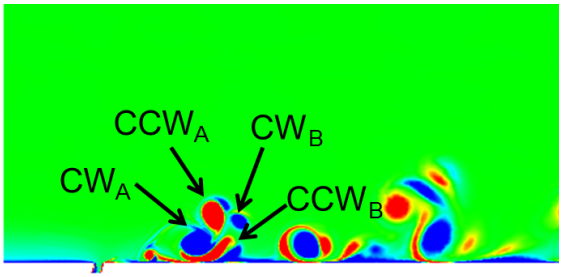

(c) Phase 288

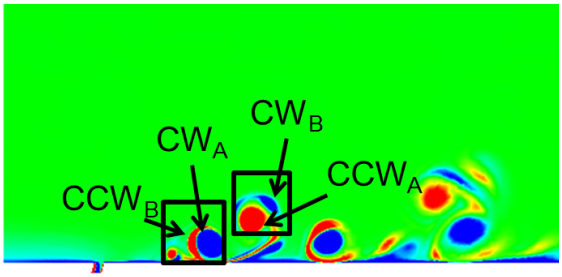

(d) Phase 360

Figure 19: Splitting of vortex pair for $\theta = 75^o$, C_b=1.0, $\hat{f}_{jet}$=0.05

More complex behavior is observed for the case with $\theta = 90^o$. At the first instance in Figure 20, the shearing of the vortex pair is shown with the help of black box. However, two distinct pairs of counter-rotating vortices are not observed. In the next instance, the initial counter-clockwise vortex is shown to have split, but the clockwise vortex is still intact. By the last instance, the clockwise vortex (CW_A) has paired

with one of the counter-clockwise vortices (CCW_A), and the remaining counter-clockwise vortex (CCW_B) is not paired with any vortex.

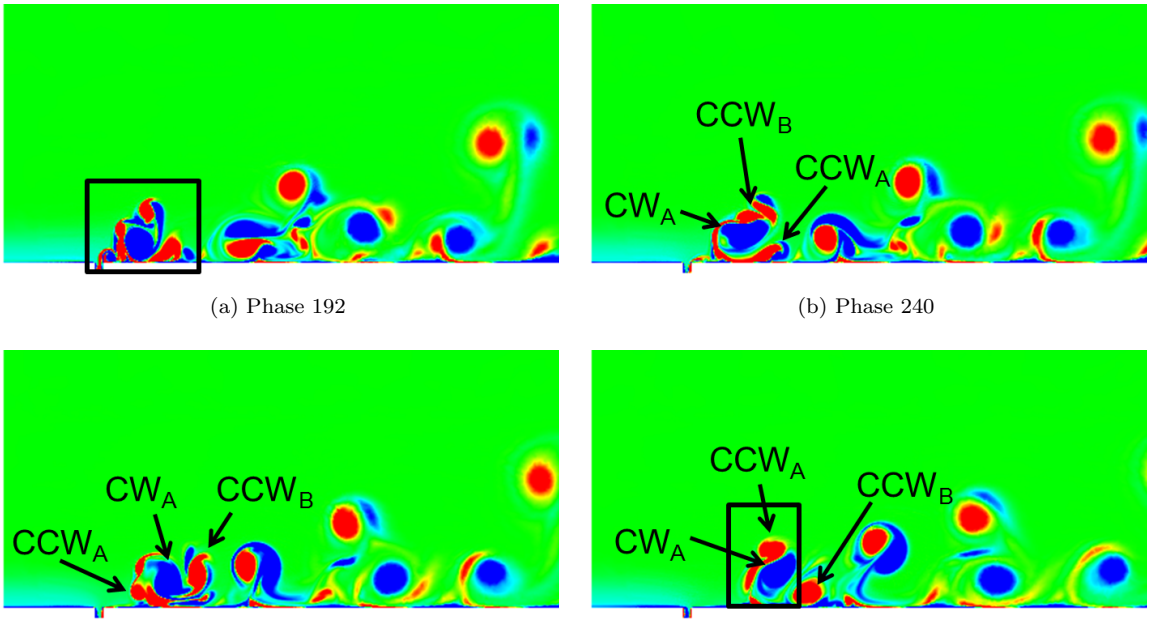

(a) Phase 192

(b) Phase 240

(c) Phase 288

(d) Phase 360

Figure 20: Splitting of vortex pair for $\theta = 90^o$, C_b=1.0, $\hat{f}_{jet}$=0.05

III.E. Complex Vortex Interactions

For high blowing ratios, complex vortex interactions are observed, as illustrated in Figure 21. Here, multiple vortex pairs from different jet cycles interact with each other. This involves different types of interactions including pair switching, splitting, subharmonics, and potentially other behaviors and structures. The combination of these different behaviors and structures result in complex structures and behaviors observed in downstream locations from the jet. This phenomenon is due to the high blowing ratio because the jet introduces large perturbations into the crossflow, causing complex interactions between the crossflow and the jet. Figure 22, Figure 23, and Figure 24 each show the ends of two consecutive jet cycles for C_b=2.0 and $\hat{f}_{jet}$=0.1, and no distinct pattern is observed.

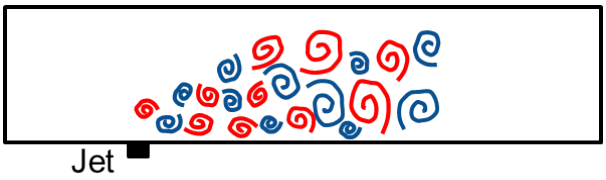

Figure 21: Depiction of complex vortex interactions

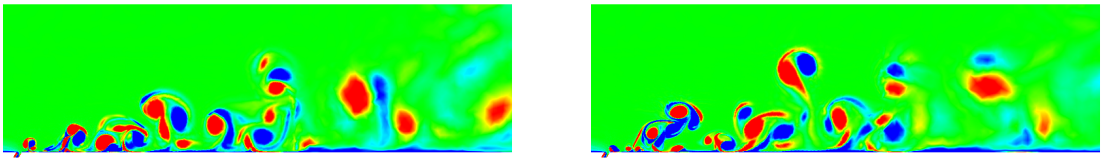

(a) Cycle A, Phase 360

(b) Cycle B, Phase 360

Figure 22: Complex vortex interactions for $\theta = 60^o$, C_b=2.0, $\hat{f}_{jet}$=0.1

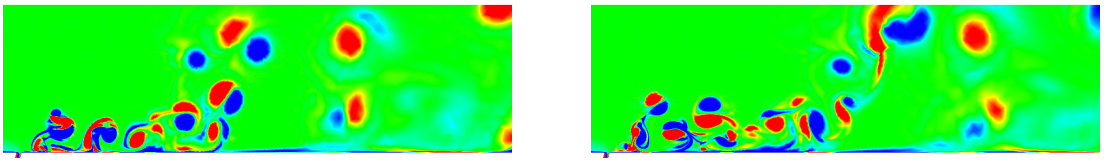

(a) Cycle A, Phase 360 (b) Cycle B, Phase 360

Figure 23: Complex vortex interactions for $\theta = 75^o$, C_b=2.0, $\hat{f}_{jet}$=0.1

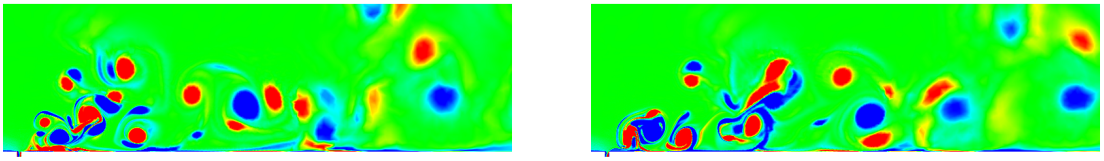

(a) Cycle A, Phase 360 (b) Cycle B, Phase 360

Figure 24: Complex vortex interactions for $\theta = 90^o$, C_b=2.0, $\hat{f}_{jet}$=0.1

III.F. Extension to 3D

For a synthetic jet in crossflow in 3D, it has been shown by Sahni et al.[10] that, despite the 3D nature of the problem, 2D structures are observed near the jet. However, is not clear whether the above structures and behaviors still exist in 3D. Therefore, 3D simulations, with an infinite-span jet and a domain with a span of $5d$, are performed for all the behaviors and structures discussed previously except for complex vortex interactions. This is done for a particular value of pitch angle for which the specific type of interaction is most prominent or clear.

III.F.1. Discrete Train of Vortex Pairs

Similar behavior is observed for a discrete train of vortex pairs in 3D. The pair of counter-rotating vortex pairs are formed and are advected by the crossflow, dissipating as they travel further downstream, see Figure 25 with vorticity contours shown at the center-plane. This behavior is similar to the one observed in 2D simulations (including the vertical extent of vortex pairs and spacing between them).

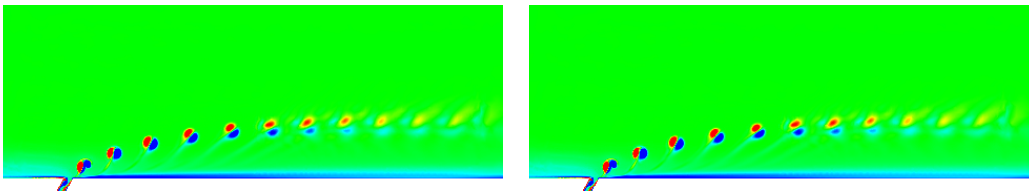

(a) Cycle A, Phase 360 (b) Cycle B, Phase 360

Figure 25: Discrete train of vortex pairs for $\theta = 60^o$, C_b=0.5, $\hat{f}_{jet}$=0.2 in 3D

III.F.2. Subharmonics

Subharmonic behavior is observed in 3D as well, as shown in Figure 26. The vortical structures downstream from the newly formed vortex structure pair are not common between Cycles A and B, but they are common between Cycles A and C. The same holds true for the structures of Cycles B and D.

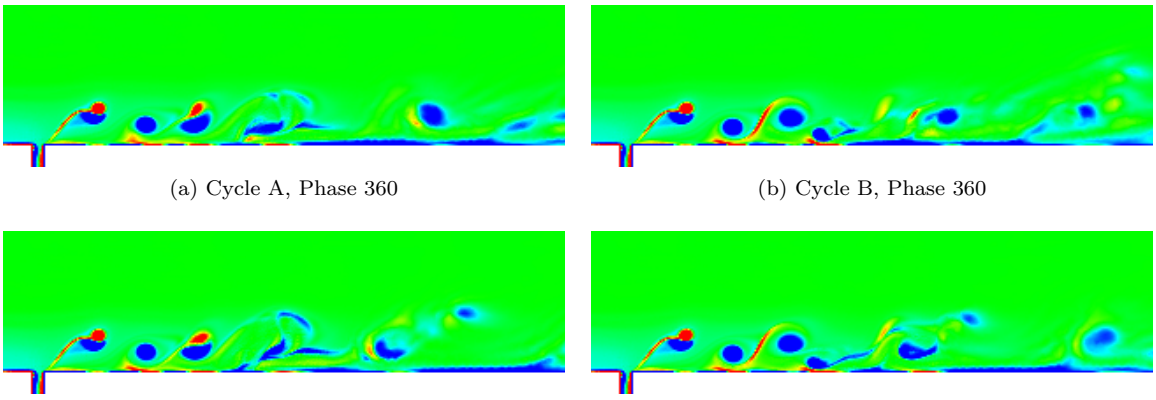

(a) Cycle A, Phase 360

(b) Cycle B, Phase 360

(c) Cycle C, Phase 360

(d) Cycle D, Phase 360

Figure 26: Subharmonics for $\theta = 90^o$, C_b=0.5, $\hat{f}_{jet}$=0.1 in 3D

III.F.3. Vortex Pair Switching

Pair switching is also observed in 3D. Following the same notation used in 2D, the first instance of Figure 27 shows the newly formed pair CCW2 and CW2 as well as CW1 from the previous jet cycle. In the next instance, the initial pair has already separated and CCW2 appears to pair with CW1. The new pair travels downstream away from CW2 in the instance after, and, at the last instance, it is clear that the pair CCW2 and CW1 (shown in the black box) are traveling further away from CW2 (indicating the separation between CCW2 and CW2).

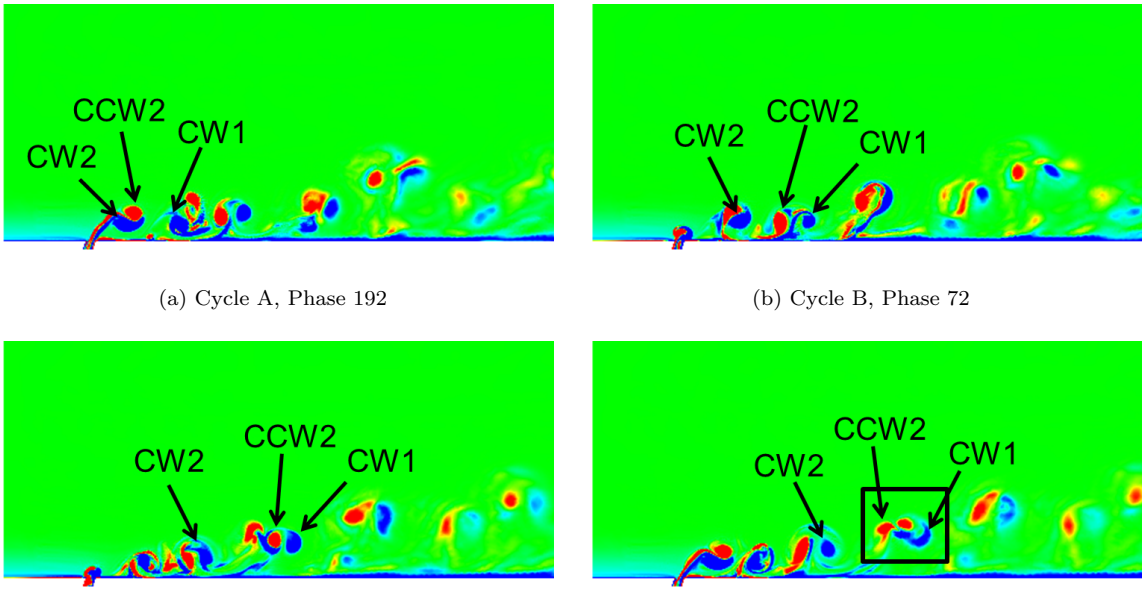

(a) Cycle A, Phase 192

(b) Cycle B, Phase 72

(c) Cycle C, Phase 48

(d) Cycle C, Phase 192

Figure 27: Switching of vortex pair for $\theta = 75^o$, C_b=1.0, $\hat{f}_{jet}$=0.1 in 3D

III.F.4. Vortex Splitting

In 3D, the vortex pairs are split into many smaller vortices and do not exhibit the alternating rotation arrangement clearly, as demonstrated in Figures 28. In the first instance, the vortex pair is already broken down into many smaller vortices. Throughout the remainder of the instances, the vortices breakdown even further resulting in finer structures. This indicates that three dimensionality plays an important role for this setting of jet parameters.

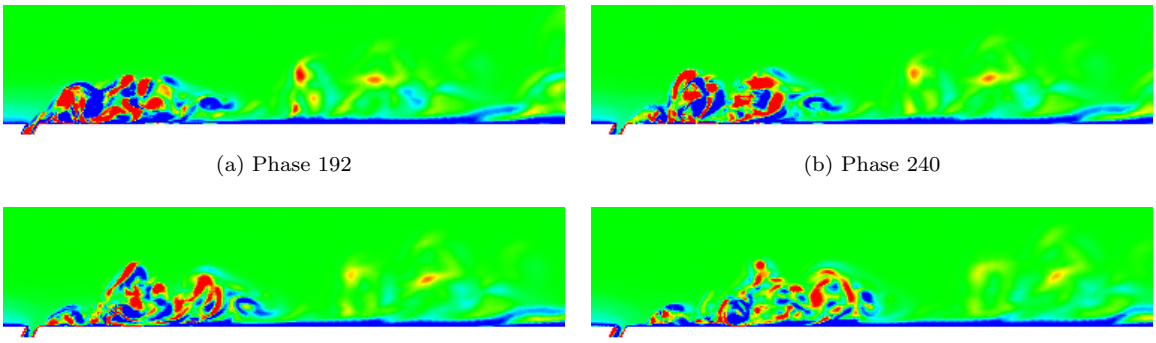

(a) Phase 192 (b) Phase 240

(c) Phase 288 (d) Phase 360

Figure 28: Splitting of vortex pair for $\theta = 60^o$, C_b=1.0, $\hat{f}_{jet}$=0.05 in 3D

IV. Closing Remarks

Different flow structures and behaviors are observed and studied for different combinations of θ, C_b, and $\hat{f}_{jet}$. In particular, five structures and behaviors are studied based on 2D simulations: a discrete train of vortex pairs, subharmonic behavior of vortex structures, vortex pair switching, vortex splitting, and complex vortex interactions. In addition, the 3D extension of these simulations (except for complex vortex interactions) indicate that such flow structures are present in 3D as well, at least in regions near the jet.

Future work will consist of understanding the effects of actuation parameters on virtual aeroshaping. Different flow frequencies that arise due to synthetic jet and crossflow interactions will be analyzed further in order to quantify the frequencies present in the flow. Also, these simulations will be extended to cases with a finite-span synthetic jet (i.e., with corner/edges effects) to observe whether or not these structures and behaviors will still be present in those cases. We also plan to consider such interactions for synthetic jet places in a turbulent boundary layer.

Acknowledgments

This work has been supported by a research grant under NASA's New York Space Grant program. SCOREC and CCI computers were used to perform the simulations. *AcuSolve*$^{\text{TM}}$ software provided by Altair engineering Inc. was used for flow simulations and *MeshSim* software provided by Simmetrix Inc. was used for mesh generation. *Paraview* software by Kitware, Inc. was used for visualization and post-processing. Max Schneider (undergraduate student) assisted greatly in this work for running and processing simulations.

References

[1]Amitay, M. and Glezer, A. (2002). Role of Actuation Frequency in Controlled Flow Reattachment over a Stalled Airfoil. *AIAA, 40, No. 2*, 209-216.

[2]Anders, S., Sellers III, W., and Washburn, A. (2004). Active Flow Control Activities at NASA Langley. *AIAA Flow Control Conference*. Portland: OR.

[3]Cattafesta III, L. and Sheplak, M. (2011). Actuators for Active Flow Control. *Annual Review of Fluid Mechanics, 43*, 247-272.

[4]Clingman, D. (2006). Development of an Aerodynamic Synthetic Jet Actuator Based on a Piezoceramic Buckled Beam. *Master's Thesis, Department of Aerospace Engineering, University of Maryland, College Park.*

[5]Glezer, A. and Amitay, M. (2002). Synthetic Jets. *Annual Review of Fluid Mechanics, 34*, 503-529.

[6]Holman, R., Uttukar, Y., Mittal, R., Smith, B. L., and Cattafesta, L. (2005). Formation Criterion for Synthetic Jets. *AIAA, 43*, 2110-2116.

[7]Honohan, A. M., Amitay, M., and Glezer, A. (2000). Aerodynamic Control using Synthetic Jets. *AIAA Paper 2000-2401.*

[8]Jansen, K. E., Whiting, C. H. , and Hulbert, G. M. (2000). A Generalized Alpha Method for Integrating the Navier-Stokes Equations with a Stabilized Finite Element Method. *Computer Methods in Applied Mechanics and Engineering, 190*, 305-319.

[9]Mittal, R. and Rampunggoon, P. (2002). On the Virtual Aeroshaping Effect of Synthetic Jets. *Physics of Fluids, 14*, 1533-1536.

[10]Sahni, O., Wood, J., Jansen, K. E., Amitay, M. (2011). Three-dimensional Interactions between a Finite-span Synthetic Jet and a Crossflow. *Journal of Fluid Mechanics, 671*, 254-287.

[11]Collis, S. S., Joslin, R. D., Seifert, A., and Theofilis, V. (2004). Issues in Active Flow Control: Theory, Control, Simulation, and Experiment. *Progress in Aerospace Sciences, 40*, 237-289.

[12]Smith, B. L., and Glezer A. (1997). Vectoring and Small-scale Motions Effected in Free Shear Flows using Synthetic Jet Actuators. *AIAA Paper 97-0213*.

[13]Whiting, C., and Jansen, K. (2001). A Stabilized Finite Element Formulation for the Incompressible Navier-Stokes Equations Using a Hierarchical Basis. *International Journal of Numerical Methods in Fluids, 35*, 93-116.